Two-Component Dynamics and the Liquidlike to Gaslike Crossover in Supercritical Water

Peihao Sun[*,†] and J. B. Hastings
SLAC National Accelerator Laboratory, 2575 Sand Hill Road, Menlo Park, California 94025, USA

Daisuke Ishikawa and Alfred Q. R. Baron
Materials Dynamics Laboratory, RIKEN SPring-8 Center, 1-1-1 Kouto, Sayo, Hyogo 679-5148, Japan

Giulio Monaco[‡]
Dipartimento di Fisica, Università di Trento, I-38123 Povo (Trento), Italy

(Received 31 July 2020; accepted 4 November 2020; published 14 December 2020)

Molecular-scale dynamics in sub- to supercritical water is studied with inelastic x-ray scattering and molecular dynamics simulations. The obtained longitudinal current correlation spectra can be decomposed into two main components: a low-frequency (LF), gaslike component and a high-frequency (HF) component arising from the O-O stretching mode between hydrogen-bonded molecules, reminiscent of the longitudinal acoustic mode in ambient water. With increasing temperature, the hydrogen-bond network diminishes and the spectral weight shifts from HF to LF, leading to a transition from liquid- to gaslike dynamics with rapid changes around the Widom line.

DOI: 10.1103/PhysRevLett.125.256001

The supercritical state of water was discovered almost 200 years ago [1], but there were few subsequent studies for a long time due to experimental challenges. In recent years, however, interest in supercritical water has been growing. This is not only because of its natural occurrence around hydrothermal vents [2,3] and in the Earth's mantle [4], which are of biological and geological importance, respectively, but also because of its wide application in biochemical technologies, such as green materials synthesis [5], biofuel production [6], and industrial waste treatment [7]. Underlying many of these applications is the large tunability of density and solvation properties near the critical point [6,8]. For water, in particular, as temperature increases in the near-critical region, its solubility for inorganic ionic compounds decreases rapidly, while many simple organic compounds and gases become soluble or even completely miscible in supercritical water [6]. These properties have been and can be further exploited to facilitate a variety of chemical processes [6,9].

From a physical viewpoint, supercritical fluids have attracted attention recently because evidence suggests the existence of "liquidlike" and "gaslike" states beyond the critical point [10,11]. A number of recent studies have thus focused on the transition between the two; in particular, the "Widom line" (WL), defined as the line of maximum correlation length in the supercritical region [12], has been proposed as a liquid-gas separatrix [13–16]. Another school of thought focuses on dynamics and proposes a separate "Frenkel line" as the border between liquid- and gaslike states [17,18]. Still another viewpoint, specific to water, focuses on the hydrogen-bond (H-bond) network structure and its related percolation threshold [19,20]. Meanwhile, the uniqueness of these boundaries has been called into question [21]. Therefore, in this Letter, we elucidate the liquid- to gaslike crossover in supercritical water by investigating angstrom-scale dynamics via inelastic x-ray scattering (IXS) and molecular dynamics (MD) simulations.

IXS measurements were carried out at BL43LXU [22] of the RIKEN SPring-8 Center in Japan. We used the Si(999) reflection with 17.8 keV incident x rays. The resolution function was measured with a 2 mm plexiglass sample and had a full width at half maximum of approximately 3 meV for all of the 20 analyzers used in the experiment. The sample length was 1.85 mm in a pressure cell with diamond windows specifically designed for use with supercritical water [23]. We scanned from −40 to 40 meV in photon energy transfer, and each scan took approximately 1.5 h, during which the temperature and pressure were controlled within ±5 K and ±10 bar. Background from the empty cell with windows was measured and subtracted, though it was negligible in the frequency range of interest.

MD simulations are carried out using the LAMMPS simulation package [24]. We use *NPT* ensembles with 2880 water molecules. After equilibration at each *P*-*T* state, the simulation is run for 1 ns at 1 fs time steps. We choose the TIP4P/2005 potential [25], which is shown to best reproduce the physical properties of water among similar models [26]; in particular, the critical temperature and density are closest to experimental values. Even though its

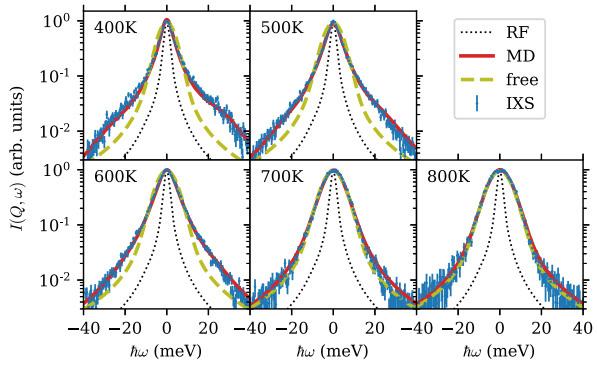

FIG. 1. Comparison of IXS data (dots with error bar) and MD simulation results (solid line) at 300 bar for $Q \approx 12$ nm^{-1}. The MD results are multiplied by the Bose factor and convolved with the RF (dotted line). The free-gas limit (dashed line) is also plotted for comparison. All spectra are scaled to match at the center ($\omega = 0$).

critical pressure, $P_c^{\mathrm{MD}} = 146$ bar, is lower than the experimental value $P_c = 221$ bar by 75 bar, it is found that the TIP4P/2005 model can reproduce many dynamic and thermodynamic properties of supercritical water with a simple pressure change [15]. Therefore, we apply a 75 bar shift in our simulations to match experimental conditions, and this shift is implied in the discussions below.

In IXS, after background substraction, the scattered intensity at momentum transfer $\hbar Q$ and energy transfer $\hbar\omega$ is [27,28]

$$I(Q,\omega) = I_0[R(\omega)] * [B(\omega)S(Q,\omega)]. \tag{1}$$

Here $*$ denotes convolution, I_0 is an overall intensity factor, $R(\omega)$ is the instrument resolution function (RF), $B(\omega)$ is the Bose factor arising from detailed balance, which for liquids is generally taken to be $B(\omega) = (\hbar\omega/k_BT)/(1 - e^{-\hbar\omega/k_BT})$ [27,28], and $S(Q,\omega)$, the *classical* dynamic structure factor, is the main quantity with which we are concerned. Because the IXS signal is dominated by scattering from oxygen atoms, we include only oxygen atoms when calculating $S(Q,\omega)$ from the MD trajectories.

For ease of discussion, we first focus on the isobar $P = 300$bar (225 bar for MD). Figure 1 presents a comparison between the measured IXS spectra and MD simulation results calculated from Eq. (1). Features in the IXS data are well reproduced by the MD model. In particular, at 400 K, both MD and IXS results show clear side bumps around ± 25 meV. At $Q = 12$ nm^{-1}, they correspond to a sound speed of approximately 3 km/s, almost twice as fast as the ultrasonic value of 1.57 km/s. This is similar to what has been measured before in ambient water [29,30] and hence suggests liquidlike dynamics. With increasing temperature, these side bumps diminish, while the central peak broadens. By 800 K, the spectrum becomes very close to the ideal-gas limit (see, e.g., Sec. 4.3 of Ref. [31]),

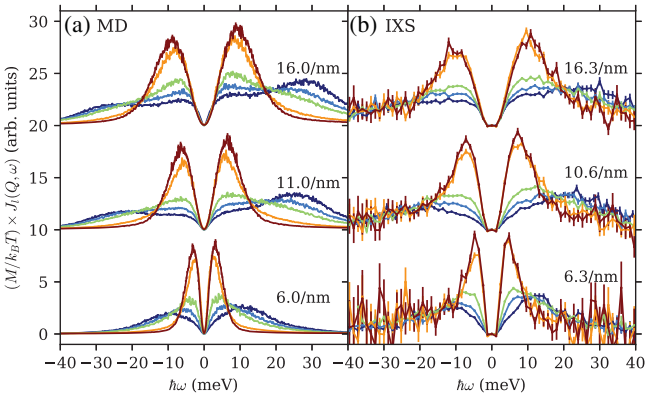

FIG. 2. Longitudinal current correlation function $J_l(Q,\omega)$ for $P = 300$ bar obtained from (a) MD and (b) IXS. MD spectra are multiplied by the Bose factor. IXS spectra are multiplied by ω^2/Q^2 after subtracting out a scaled RF (see Supplemental Material [32]). The spectra from dark blue to dark red are taken from 400 to 800 K at 100 K steps. An offset is applied between different spectra at different Q values as indicated in the plots.

$$S(Q,\omega) = \frac{1}{\sqrt{2\pi}Qv_0}\exp\left[-\frac{1}{2}\left(\frac{\omega}{Qv_0}\right)^2\right], \tag{2}$$

where $v_0 \equiv \sqrt{k_BT/M}$ is the thermal velocity and M is the molecular mass of water.

To better investigate this liquid- to gaslike transition n the dynamics, we focus on the longitudinal current-current correlation function $J_l(Q,\omega)$, which is often used to investigate acoustic modes at finite wavelengths. It can be shown that $J_l(Q,\omega)$ bears a simple relation to $S(Q,\omega)$ [31],

$$J_l(Q,\omega) = \frac{\omega^2}{Q^2}S(Q,\omega). \tag{3}$$

Moreover, because of the sum rule [31] $\int_{-\infty}^{\infty} J_l(Q,\omega)d\omega = k_BT/M$, $J_l(Q,\omega)$ can be conveniently normalized with a factor M/k_BT, making it easy to quantify spectral components, as will be shown below. The normalized J_l spectra are presented in Fig. 2. The MD spectra are multiplied by the Bose factor, which reproduces the enhanced IXS signal on the Stokes ($\omega > 0$) side. To obtain J_l from IXS data, we multiply the IXS intensities by ω^2/Q^2 and subtract the quasielastic background, which becomes significant near the critical point (see Supplemental Material [32]). Again, details of the temperature evolution in the IXS data are well reproduced in the MD results.

Upon closer examination, two distinct components can be seen in J_l: a low-frequency (LF) component peaked below 10 meV and a high-frequency (HF) component peaked around 25 meV. While the HF component corresponds to the side bumps at lower temperatures in Fig. 1, thus representing liquidlike dynamics, the LF component eventually becomes the ideal-gas-like spectrum at high

temperatures. With increasing temperature, the spectral weight shifts from HF to LF, leading to a crossover from liquid- to gaslike dynamics.

Having established the phenomenology for the dynamic crossover, we now quantify this transition and find its physical origin. To our knowledge, however, no theory to date can fully reproduce the spectra shown in Fig. 2. Fitting with given spectral shapes such as damped harmonic oscillators [29,30,33] or the memory function [27,34,35], as is usually done in IXS data analyses, results in large fluctuations in the fit parameters. In addition, the physical motivation behind these fit models—the existence of acoustic modes—is lost at high temperatures when the fluid becomes gaslike. Therefore, we take a phenomenological approach and use non-negative matrix factorization (NMF), which is model independent and has been shown to give parts-based representations of data when properly constrained [36]. Mathematically, we optimize the decomposition

$$J_l(Q,\omega;P,T) = f_{\mathrm{HF}}(P,T)J_l^{\mathrm{HF}}(Q,\omega) + f_{\mathrm{LF}}(P,T)J_l^{\mathrm{LF}}(Q,\omega) \quad (4)$$

and find the PT-independent components J_l^{HF} and J_l^{LF}, as well as their weights f_{HF} and f_{LF} for each thermodynamic state. The non-negative double singular value decomposition initialization [37] is used to facilitate the separation of the components, although other initializations in Ref. [37] lead to essentially the same results. Data below 6 nm^{-1} are excluded to avoid the influence from critical fluctuations (large quasielastic scattering intensities as seen in, e.g., Refs. [34] and [35]). The data in the Q range 6–18 nm^{-1} are fit simultaneously, i.e., with the same weights f_{HF} and f_{LF}. This is found to give consistent results. Moreover, because of the aforementioned sum rule for J_l, we may normalize the components J_l^{HF} and J_l^{LF} so they both have the same area as J_l. Then, $f_{\mathrm{HF}} + f_{\mathrm{LF}} = 1$ for each PT state, and in the following discussion we use $f \equiv f_{\mathrm{HF}}$ to denote the fraction of the HF component. We note that this decomposition scheme is conceptually similar to the two-phase thermodynamic model proposed by Lin *et al.* [38,39] and the low-frequency fraction $f_{\mathrm{LF}} = 1 - f$ is analogous to the translational "fluidicity" parameter defined therein. However, our method avoids the need to find a reference hard-spheres system and, as discussed below, the ability to examine the Q dependence helps provide insight into the nature of the LF and HF components.

Figures 3(a) and 3(b) present the NMF results for the spectra shown in Fig. 2 after dividing out the Bose factor. The shapes and temperature dependence of both components are discernible. In Fig. 3(c), it can be seen that the fraction of the HF component f obtained from MD and IXS closely follow each other, and both decrease monotonically as temperature increases. The presence of the WL is visible as a sudden drop in f as temperature rises. This becomes clearer when we look at the derivative $|df/dT|$, calculated using the finite difference approximation, and compare it

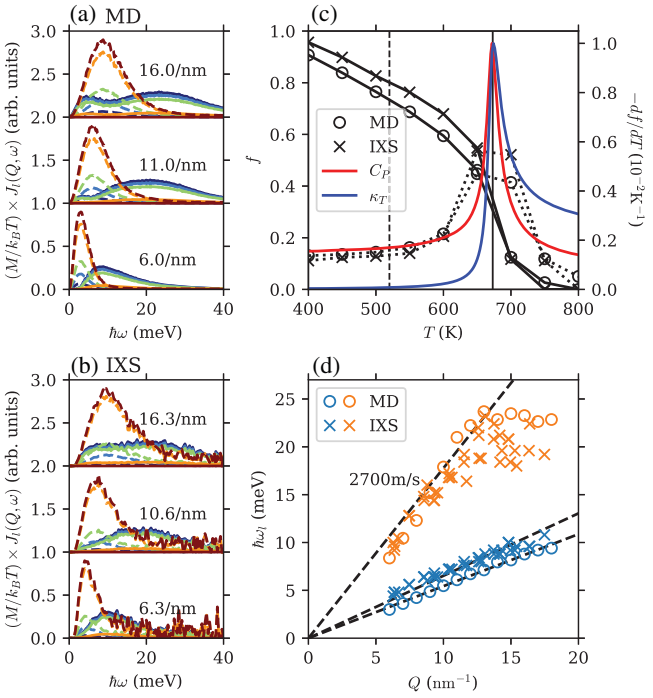

FIG. 3. NMF results. (a) Dashed and solid lines indicate the LF and HF components of the MD spectra; (b) the same for IXS spectra. Color schemes and Q values are the same as in Fig. 2. (c) Circles, MD; crosses, IXS. Black solid lines show fraction of the HF component as a function of temperature (see text), while dotted lines show their temperature derivatives; these lines are guides to the eye. Also plotted are C_P (red) and κ_T (blue) scaled to match the derivatives. Solid and dashed vertical lines indicate the approximate position of the Widom line (maximum of C_P and κ_T) and the Frenkel line [18], respectively. (d) Dispersion curves for peak frequencies of the LF (blue) and HF (orange) components. Symbols are the same as in (c); dashed lines indicate linear dispersions.

with thermodynamic response functions such as isobaric heat capacity C_P and isothermal compressibility κ_T. Thus, f can be used to describe the dynamic crossover in the supercritical region and is tied closely to thermodynamic properties. Because the analysis and discussion so far are not specific to water, the close connection between dynamics and thermodynamics may be applicable to other fluid systems exhibiting the two-component behavior. A possible candidate is liquid Te which, similar to water, shows a large positive sound dispersion close to its melting point [40]. We note in passing that the Frenkel line given in Ref. [18] does not appear to correspond to significant changes in the dynamics, as shown in Fig. 3(c).

In order to identify the microscopic origin of the dynamic transition, it is helpful to examine the dispersion relations $\omega_l(Q)$ for the HF and LF components, where the mode frequency ω_l is defined as the peak frequency at a given Q. The results are shown in Fig. 3(d). For the LF component, ω_l changes linearly with Q, as expected for an ideal gas (see Supplemental Material [32]). The HF component, on the other hand, has a Q dependence

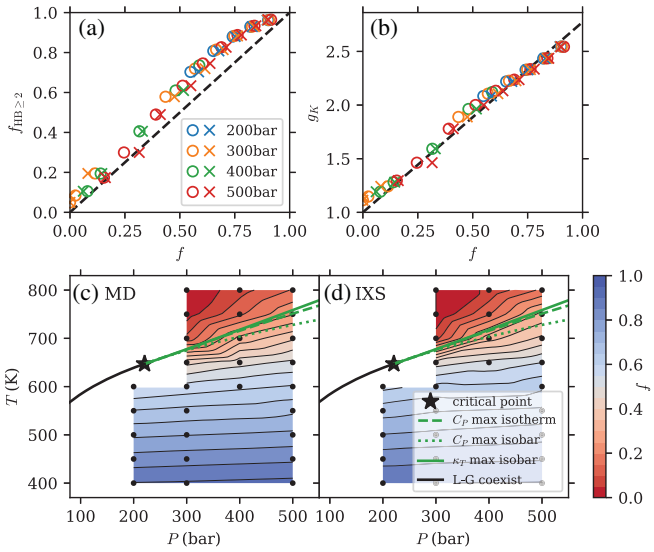

FIG. 4. Fraction of the HF component f plotted against (a) the fraction of molecules with two or more H bonds, $f_{\mathrm{HB}\geq 2}$, and (b) the Kirkwood correlation factor g_K. Circles, MD; crosses, IXS. Different colors indicate different isobars as shown in the legend. (c),(d) Contour plots for f on the water phase diagram from MD and IXS, respectively. Black dots indicate states where data are taken; the contour plot is made by linear interpolation on these data. Also plotted are the critical point (black star), liquid-gas coexistence line (black line), and Widom lines by various definitions (green lines; see legend). Thermodynamic data are obtained from the IAPWS-95 equation of state [54].

characteristic of acoustic modes: it disperses linearly with Q until it flattens around 12 nm^{-1}, i.e., near the boundary of the pseudo-Brillouin zone [33], which closely resembles the longitudinal acoustic branch observed in ambient liquid water [30,41]. Notice also that the peak frequency near the zone boundary is around 25 meV (200 cm^{-1}), recalling earlier Raman and far-IR measurements in which a peak at similar position was seen [42–44]. Based on earlier studies on this peak [43,45–48] and the fact that our study is sensitive only to oxygen atoms, we identify the nature of the HF component as the longitudinal acoustic excitation which, with increasing Q, converges to the O-O stretching motion between H-bonded molecules. The decrease of f is then naturally related to the diminishing of the H-bond network.

In Fig. 4(a), we plot the parameter f against the fraction of molecules with two or more H bonds, $f_{\mathrm{HB}\geq 2}$, obtained from MD results. Here we use a H-bond definition common in the literature: two molecules are H bonded if their O-O distance is less than 3.5 Å and the O$\cdots$O-H angle is less than 30° [49,50]. We note that, even though different definitions result in different H-bond populations [51–53], they lead to the same conclusions (see Supplemental Material [32]). As shown in Fig. 4(a), the data collapse onto a single line with an almost 1:1 ratio, indicating a strong correlation between f and the fraction of $\geq$ 2-bonded molecules in the probed P-T range. We interpret this as evidence to identify molecules giving rise to the HF component with $\geq$ 2-bonded molecules that are in the body of the H-bond network and those contributing to the LF component with monomers and singly bonded molecules in the periphery of the H-bond clusters.

The close relation between f and H bonding suggests that f may also be connected to chemical properties of sub- to supercritical water. Here we focus on the dielectric constant ε which controls the solvation behavior and is thus relevant for many chemical processes [9,55]. Notably, ε decreases from around 80 under ambient conditions to about 6 near the critical point—a value close to that of organic solvents—and is thus able to dissolve many organic molecules [6,9]. A widely used model for ε is the Kirkwood-Fröhlich equation [55–58]

$$\frac{(\varepsilon - n^2)(2\varepsilon + n^2)}{\varepsilon(n^2+2)^2} = g_K \frac{\rho\mu^2}{9M\varepsilon_0 k_B T}, \tag{5}$$

where $\mu = 1.8546$ D is the gas-phase dipole moment of water [59] and ε_0 is the vacuum permittivity. n is the refractive index at the reference wavelength $\lambda = 0.589$ μm [60]; we have checked that choosing $\lambda = 1.1$ μm leads to the same results. The so-called Kirkwood correlation factor g_K is defined as the ratio of the total dipole moment in a spherical volume surrounding a fixed molecule to the dipole moment of that molecule, in the absence of external fields. Thus, $g_K = 1$ if there is no intermolecular correlation (as expected for a gas), and $g_K > 1$ if molecular dipoles tend to align in parallel (as in room temperature water). This definition suggests a close relation between g_K and the parameter f in our study. To demonstrate, we calculate g_K using Eq. (5) and plot it against f in Fig. 4(b). Indeed, good linearity exists between these two parameters. Moreover, the data are consistent with an intercept at $g_K = 1$ for $f = 0$, where gaslike behavior is expected. Hence we show as a dashed line a linear fit fixing the intercept at $g_K = 1$. The fit indicates $g_K = 2.77$ when $f = 1$, i.e., in the absence of the LF component, which is remarkably close to the value $g_K = 2.79$ at ambient conditions (1 bar, 300 K). Therefore, we have established a close relation between f and g_K; since the latter is tied to the dielectric constant and is suggested to influence transport properties as well [61], the parameter f can be viewed as a directly measurable quantity that characterizes chemical properties of supercritical water.

For an overview of the dynamic crossover, in Figs. 4(c) and 4(d) we show contour maps of f on the phase diagram. The topology is clearly influenced by the Widom line, which traces the loci of the highest gradients, indicating rapid shifts between liquid- and gaslike dynamics. However, we emphasize that remnants of the HF component can be found above the Widom line and the LF component below, thus supporting the view of the Widom line as an indicator of continuous crossover instead of a rigid separatrix between distinct liquid- and gaslike phases [21].

In conclusion, we have used a combination of IXS measurements and MD simulations to study the crossover

from liquid- to gaslike dynamics in supercritical water. The TIP4P/2005 model for MD well reproduces the intermolecular dynamics measured via IXS. We find that the dynamics can be separated into liquidlike (HF) and gaslike (LF) components, and it is the changing ratio between the two that leads to the crossover. Through further analysis, we find a strong correlation between the fraction of the HF component and molecules with two or more H bonds, which is significant for modeling of solvent properties such as the dielectric constant. The Widom line, which originates from thermodynamic properties, coincides with rapid changes in the intermolecular dynamics and H bonding as well.

This work is supported by the U.S. Department of Energy, Office of Science, Office of Basic Energy Sciences under Contract No. DE-AC02-76SF00515. The inelastic x-ray scattering measurements were performed at the Quantum NanoDynamics Beamline, BL43LXU, of the RIKEN SPring-8 Center. We would like to thank Stanford University and the Stanford Research Computing Center for providing computational resources and support that contributed to this work.

*phsun@stanford.edu
†Also at Stanford University Physics Department, 382 Via Pueblo Mall, Stanford, California 94305, USA.
‡Present address: Dipartimento di Fisica ed Astronomia, Università di Padova, 35131 Padova, Italy.

[1] C. Cagniard de la Tour, Exposé de quelques résultats obtenus par l'action combinée de la chaleur et de la compression sur certains liquides, tels que l'eau, l'alcool, l'éther sulfurique et l'essence de pétrole rectifiée, Ann. Chim. Phys. **21**, 127 (1822), http://sciences.amisbnf.org/fr/livre/expose-de-quelques-resultats-obtenus-par-laction-combinee-de-la-chaleur-et-de-la-compression.
[2] B. R. T. Simoneit, Aqueous high-temperature and high-pressure organic geochemistry of hydrothermal vent systems, Geochim. Cosmochim. Acta **57**, 3231 (1993).
[3] W. Martin, J. Baross, D. Kelley, and M. J. Russell, Hydrothermal vents and the origin of life, Nat. Rev. Microbiol. **6**, 805 (2008).
[4] M. Hirschmann and D. Kohlstedt, Water in Earth's mantle, Phys. Today **65**, No. 3, 40 (2012).
[5] T. Adschiri, Y.-W. Lee, M. Goto, and S. Takami, Green materials synthesis with supercritical water, Green Chem. **13**, 1380 (2011).
[6] A. A. Peterson, F. Vogel, R. P. Lachance, M. Fröling, M. J. Antal, Jr., and J. W. Tester, Thermochemical biofuel production in hydrothermal media: A review of sub- and supercritical water technologies, Energy Environ. Sci. **1**, 32 (2008).
[7] M. D. Bermejo and M. J. Cocero, Supercritical water oxidation: A technical review, AIChE J. **52**, 3933 (2006).
[8] C. A. Eckert, B. L. Knutson, and P. G. Debenedetti, Supercritical fluids as solvents for chemical and materials processing, Nature (London) **383**, 313 (1996).
[9] N. Akiya and P. E. Savage, Roles of water for chemical reactions in high-temperature water, Chem. Rev. **102**, 2725 (2002).
[10] A. Cunsolo, G. Pratesi, G. Ruocco, M. Sampoli, F. Sette, R. Verbeni, F. Barocchi, M. Krisch, C. Masciovecchio, and M. Nardone, Dynamics of Dense Supercritical Neon at the Transition from Hydrodynamical to Single-Particle Regimes, Phys. Rev. Lett. **80**, 3515 (1998).
[11] F. Gorelli, M. Santoro, T. Scopigno, M. Krisch, and G. Ruocco, Liquidlike Behavior of Supercritical Fluids, Phys. Rev. Lett. **97**, 245702 (2006).
[12] L. Xu, P. Kumar, S. V. Buldyrev, S.-H. Chen, P. H. Poole, F. Sciortino, and H. E. Stanley, Relation between the Widom line and the dynamic crossover in systems with a liquid liquid phase transition, Proc. Natl. Acad. Sci. U.S.A. **102**, 16558 (2005).
[13] P. F. McMillan and H. E. Stanley, Going supercritical, Nat. Phys. **6**, 479 (2010).
[14] G. G. Simeoni, T. Bryk, F. A. Gorelli, M. Krisch, G. Ruocco, M. Santoro, and T. Scopigno, The Widom line as the crossover between liquid-like and gas-like behaviour in supercritical fluids, Nat. Phys. **6**, 503 (2010).
[15] P. Gallo, D. Corradini, and M. Rovere, Widom line and dynamical crossovers as routes to understand supercritical water, Nat. Commun. **5**, 5806 (2014).
[16] D. T. Banuti, Crossing the Widom-line supercritical pseudo-boiling, J. Supercrit. Fluids **98**, 12 (2015).
[17] K. Trachenko and V. V. Brazhkin, Collective modes and thermodynamics of the liquid state, Rep. Prog. Phys. **79**, 016502 (2016).
[18] C. Yang, V. V. Brazhkin, M. T. Dove, and K. Trachenko, Frenkel line and solubility maximum in supercritical fluids, Phys. Rev. E **91**, 012112 (2015).
[19] L. Pártay and P. Jedlovszky, Line of percolation in supercritical water, J. Chem. Phys. **123**, 024502 (2005).
[20] M. Bernabei, A. Botti, F. Bruni, M. A. Ricci, and A. K. Soper, Percolation and three-dimensional structure of supercritical water, Phys. Rev. E **78**, 021505 (2008).
[21] P. Schienbein and D. Marx, Investigation concerning the uniqueness of separatrix lines separating liquidlike from gaslike regimes deep in the supercritical phase of water with a focus on Widom line concepts, Phys. Rev. E **98**, 022104 (2018).
[22] A. Q. R. Baron, The RIKEN quantum nanodynamics beamline (BL43LXU): The next generation for inelastic x-ray scattering, SPring-8 Inf. Newslett. **15**, 14 (2010), https://user.spring8.or.jp/sp8info/?p=3138.
[23] D. Ishikawa, Y. Q. Cai, D. M. Shaw, J. S. Tse, N. Hiraoka, and A. Q. R. Baron, X-ray Raman scattering of water near the critical point: Comparison of an isotherm and isochore, arXiv:1210.4274.
[24] S. Plimpton, Fast parallel algorithms for short-range molecular dynamics, J. Comput. Phys. **117**, 1 (1995).
[25] J. L. F. Abascal and C. Vega, A general purpose model for the condensed phases of water: TIP4P/2005, J. Chem. Phys. **123**, 234505 (2005).
[26] C. Vega and J. L. F. Abascal, Simulating water with rigid non-polarizable models: A general perspective, Phys. Chem. Chem. Phys. **13**, 19663 (2011).

[27] G. Monaco, A. Cunsolo, G. Ruocco, and F. Sette, Viscoelastic behavior of water in the terahertz-frequency range: An inelastic x-ray scattering study, Phys. Rev. E **60**, 5505 (1999).

[28] A. Q. R. Baron, High-resolution inelastic x-ray scattering part II: Scattering theory, harmonic phonons, and calculations, in *Synchrotron Light Sources and Free-Electron Lasers*, 2nd ed., edited by E. J. Jaeschke, S. Khan, J. R. Schneider, and J. B. Hastings (Springer International Publishing, Cham, 2020), pp. 2213–2250, see also arXiv: 1504.01098.

[29] J. Teixeira, M. C. Bellissent-Funel, S. H. Chen, and B. Dorner, Observation of New Short-Wavelength Collective Excitations in Heavy Water by Coherent Inelastic Neutron Scattering, Phys. Rev. Lett. **54**, 2681 (1985).

[30] F. Sette, G. Ruocco, M. Krisch, U. Bergmann, C. Masciovecchio, V. Mazzacurati, G. Signorelli, and R. Verbeni, Collective Dynamics in Water by High Energy Resolution Inelastic X-Ray Scattering, Phys. Rev. Lett. **75**, 850 (1995).

[31] J. P. Boon and S. Yip, *Molecular Hydrodynamics* (Dover Publications, New York, 1991).

[32] See Supplemental Material at http://link.aps.org/supplemental/10.1103/PhysRevLett.125.256001 for detailed definitions of correlation functions, treatment of IXS data, enthalpy difference between the HF and LF components, and effects of the H-bond definition on the results.

[33] V. M. Giordano and G. Monaco, Fingerprints of order and disorder on the high-frequency dynamics of liquids, Proc. Natl. Acad. Sci. U.S.A. **107**, 21985 (2010).

[34] T. Yamaguchi, K. Yoshida, N. Yamamoto, S. Hosokawa, M. Inui, A. Q. R. Baron, and S. Tsutsui, Collective dynamics of supercritical water, J. Phys. Chem. Solids **66**, 2246 (2005).

[35] F. Bencivenga, A. Cunsolo, M. Krisch, G. Monaco, G. Ruocco, and F. Sette, High-frequency dynamics of liquid and supercritical water, Phys. Rev. E **75**, 051202 (2007).

[36] P. O. Hoyer, Non-negative matrix factorization with sparseness constraints, J. Mach. Learn. Res. **5**, 1457 (2004), https://www.jmlr.org/papers/volume5/hoyer04a/hoyer04a.pdf.

[37] C. Boutsidis and E. Gallopoulos, SVD based initialization: A head start for nonnegative matrix factorization, Pattern Recognit. **41**, 1350 (2008).

[38] S.-T. Lin, M. Blanco, and W. A. Goddard, The two-phase model for calculating thermodynamic properties of liquids from molecular dynamics: Validation for the phase diagram of Lennard-Jones fluids, J. Chem. Phys. **119**, 11792 (2003).

[39] S.-T. Lin, P. K. Maiti, and W. A. Goddard, Two-phase thermodynamic model for efficient and accurate absolute entropy of water from molecular dynamics simulations, J. Phys. Chem. B **114**, 8191 (2010).

[40] Y. Kajihara, M. Inui, S. Hosokawa, K. Matsuda, and A. Q. R. Baron, Dynamical inhomogeneity of liquid Te near the melting temperature proved by inelastic x-ray scattering measurements, J. Phys. Condens. Matter **20**, 494244 (2008).

[41] M. Sampoli, G. Ruocco, and F. Sette, Mixing of Longitudinal and Transverse Dynamics in Liquid Water, Phys. Rev. Lett. **79**, 1678 (1997).

[42] G. E. Walrafen, M. R. Fisher, M. S. Hokmabadi, and W. Yang, Temperature dependence of the low and high-frequency Raman scattering from liquid water, J. Chem. Phys. **85**, 6970 (1986).

[43] G. E. Walrafen, Y. C. Chu, and G. J. Piermarini, Low-frequency Raman scattering from water at high pressures and high temperatures, J. Phys. Chem. **100**, 10363 (1996).

[44] H. R. Zelsmann, Temperature dependence of the optical constants for liquid H_2O and D_2O in the far IR region, J. Mol. Struct. **350**, 95 (1995).

[45] M. Sharma, R. Resta, and R. Car, Intermolecular Dynamical Charge Fluctuations in Water: A Signature of the H-Bond Network, Phys. Rev. Lett. **95**, 187401 (2005).

[46] W. Chen, M. Sharma, R. Resta, G. Galli, and R. Car, Role of dipolar correlations in the infrared spectra of water and ice, Phys. Rev. B **77**, 245114 (2008).

[47] G. M. Sommers, M. F. Calegari Andrade, L. Zhang, H. Wang, and R. Car, Raman spectrum and polarizability of liquid water from deep neural networks, Phys. Chem. Chem. Phys. **22**, 10592 (2020).

[48] O. F. Nielsen, Chapter 3. Low-frequency spectroscopic studies and intermolecular vibrational energy transfer in liquids, Annu. Rep. Sect. C **93**, 57 (1996).

[49] A. Luzar and D. Chandler, Hydrogen-bond kinetics in liquid water, Nature (London) **379**, 55 (1996).

[50] A. Luzar and D. Chandler, Effect of Environment on Hydrogen Bond Dynamics in Liquid Water, Phys. Rev. Lett. **76**, 928 (1996).

[51] M. Matsumoto, Relevance of hydrogen bond definitions in liquid water, J. Chem. Phys. **126**, 054503 (2007).

[52] S. E. Strong, L. Shi, and J. L. Skinner, Percolation in supercritical water: Do the Widom and percolation lines coincide?, J. Chem. Phys. **149**, 084504 (2018).

[53] R. Kumar, J. R. Schmidt, and J. L. Skinner, Hydrogen bonding definitions and dynamics in liquid water, J. Chem. Phys. **126**, 204107 (2007).

[54] W. Wagner and A. Pruß, The IAPWS formulation 1995 for the thermodynamic properties of ordinary water substance for general and scientific use, J. Phys. Chem. Ref. Data **31**, 387 (2002).

[55] H. Weingärtner and E. U. Franck, Supercritical water as a solvent, Angew. Chem., Int. Ed. Engl. **44**, 2672 (2005).

[56] S. J. Suresh and V. M. Naik, Hydrogen bond thermodynamic properties of water from dielectric constant data, J. Chem. Phys. **113**, 9727 (2000).

[57] J. G. Kirkwood, The dielectric polarization of polar liquids, J. Chem. Phys. **7**, 911 (1939).

[58] H. Fröhlich, *Theory of Dielectrics: Dielectric Constant and Dielectric Loss*, Monographs on the Physics and Chemistry of Materials (Clarendon Press, Oxford, 1949).

[59] D. R. Lide, Dielectric constants, in *CRC Handbook of Chemistry and Physics*, 100th ed., edited by J. R. Rumble (CRC Press/Taylor & Francis, Boca Raton, FL, 2019).

[60] A. H. Harvey, J. S. Gallagher, and J. M. H. Levelt Sengers, Revised formulation for the refractive index of water and steam as a function of wavelength, temperature and density, J. Phys. Chem. Ref. Data **27**, 761 (1998).

[61] Y. Marcus, On transport properties of hot liquid and supercritical water and their relationship to the hydrogen bonding, Fluid Phase Equilib. **164**, 131 (1999).